

Stable and Controllable Polymer/Fullerene Composite Nanofibers through Cooperative Noncovalent Interactions for Organic Photovoltaics

Fei Li,[†] Kevin G. Yager,[#] Noel M. Dawson,[§] Ying-Bing Jiang,[‡] Kevin J. Malloy,[§] and Yang Qin^{*†}

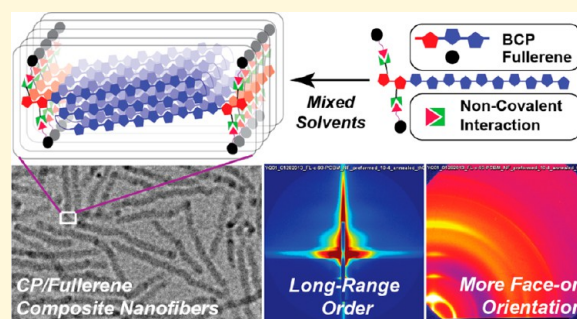
[†]Department of Chemistry & Chemical Biology and [‡]TEM Laboratory, University of New Mexico, Albuquerque, New Mexico 87131, United States

[#]Center for Functional Nanomaterials, Brookhaven National Laboratory, Upton, New York 11973, United States

[§]Center for High Technology Materials, University of New Mexico, Albuquerque, New Mexico 87106, United States

Supporting Information

ABSTRACT: A novel methodology of precisely constructing stable and controllable conjugated polymer (CP)/fullerene nanostructures is presented. By building in noncovalent interactions between CP nanofibers (NFs) and fullerene derivatives, supramolecular polymer/fullerene composite NFs are obtained in solution for the first time. Specifically, a conjugated block copolymer having poly(3-hexylthiophene) (P3HT) backbone selectively functionalized with polar isoorotic acid (IOA) moieties, **P1**, is used as the building block. Self-assembly of **P1** in mixed solvents leads to well-defined NFs decorated with IOA groups on the periphery, onto which phenyl-C61-butyric acid methyl ester (PCBM) molecules are subsequently attached noncovalently. Formation of such complex structures are studied in detail and confirmed by UV–vis absorption spectroscopy, transmission electron microscopy (TEM), atomic force microscopy (AFM), and X-ray scattering measurements. Application of these composite NFs in organic photovoltaic (OPV) devices not only leads to superior performance but also much improved thermal stability and better defined and controllable morphology, when compared with conventional bulk heterojunction (BHJ) devices.



1. INTRODUCTION

Conjugated polymers (CPs)¹ have over the past few decades become the foci of extensive research efforts and found widespread applications in modern electronic devices including organic field-effect transistors (OFETs),^{2,3} organic light emitting diodes (OLEDs),^{4,5} electrochromics,^{6,7} memory devices,^{8,9} and organic photovoltaics (OPVs).^{10–14} Specifically, OPVs derived from CPs have been considered promising alternative energy sources due to the lightweight, flexibility, and amenability to low-cost high throughput fabrication processes.^{15,16} In order for OPV technology to receive wide acceptance, both device efficiency and stability need to be further improved, for which morphology of the photoactive layer plays a decisive role.^{17–21} It has been generally recognized that an interpenetrating donor–acceptor network having phase separation on the nanometer scale is essential for efficient charge generation. Such so-called bulk heterojunction (BHJ) strategy has led to efficient OPV devices of power conversion efficiencies (PCEs) approaching and now beyond 10%.^{22–25} Typical BHJs are optimized thermally and/or via solvent annealing through trial and error approaches that are hardly predictable and highly system dependent. BHJs are intrinsically in a thermodynamically metastable state, and spontaneous macroscopic phase separation over time will eventually lead to

device degradation.^{26–29} Thus, it is highly desirable to develop general methods to construct, in precisely controlled manners, CP/fullerene nanostructures that not only are stable but also have dimensions optimal for OPV operation.^{30,31}

One such effort is centered around CP nanofibers (NFs) that have been exclusively based on poly(3-alkylthiophene)s (P3ATs), especially regioregular poly(3-hexylthiophene)s (P3HTs). Induced by strong intermolecular π – π interactions, well-defined P3AT NFs up to micrometers in length can be obtained under proper conditions. These NFs typically have widths of 10–20 nm, optimal for exciton dissociation.^{32–39} Compared with well-dissolved solutions and disordered thin films, P3AT NFs have unique device favorable properties including high crystallinity, J-type aggregation, and superior charge mobilities.^{40–44} Indeed, P3AT NFs have been incorporated into OPV devices that showed comparable or better PCEs than corresponding conventional BHJ cells.^{45–48} Additionally, conjugated block copolymers (BCPs) containing P3AT segments have recently attracted significant attention due to their ability to self-assemble into stable and more complex

Received: April 8, 2014

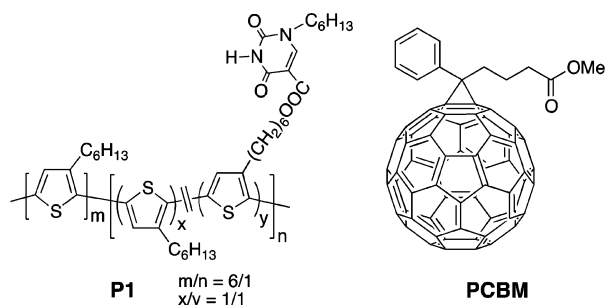
Revised: May 29, 2014

Published: May 31, 2014

nanostructures that have also been applied in efficient OPV devices.^{49–56} As such, most research efforts in this area have been devoted to nanostructure formation mechanisms and improvement of device PCEs with, however, little attention paid to morphology stability. Since such devices are typically fabricated by blending CP NFs with fullerene derivatives, between which there is no strong or specific interactions, large-scale phase separation is expected over time due to the strong aggregation tendency of fullerenes.

Herein, we report a novel strategy to precisely construct stable CP/fullerene composite NFs through cooperation of noncovalent interactions. Self-assembly of a diblock copolymer, having P3HT backbone and isoorotic acid (IOA) moieties attached to the shorter segment (poly(3-hexylthiophene-2,5-diyl)-*b*-poly(3-hexylthiophene-2,5-diyl-co-3-(1-hexyl-2,4-dioxo-1,2,3,4-tetrahydropyrimidine-5-carboxylate)-hexylthiophene-2,5-diyl), **P1**, Scheme 1), in mixed solvents led

Scheme 1. Chemical Structures of P1 and PCBM



to formation of well-defined NFs having IOA moieties on the periphery. Hydrogen bonding as well as π - π interactions between IOA moieties and phenyl-C61-butyl ester methyl ester (PCBM, Scheme 1) molecules led to selective noncovalent attachment of fullerenes onto the NFs. Such supramolecular composite NFs not only led to stable and high-performing OPV devices but also displayed better defined and controllable morphology on the nanometer scale.

2. EXPERIMENTAL SECTION

2.1. Materials and General Methods. All reagents and solvents were used as received from Sigma-Aldrich or Alfa Aesar unless otherwise noted. Phenyl-C61-butyl ester methyl ester (PCBM) was purchased from American Dye Source. Synthesis of **P1** was described previously.^{57,58} Size exclusion chromatography (SEC) analyses were performed in chloroform with 0.5% (vol./vol.) triethylamine (1 mL/min) using a Waters Breeze system equipped with a 2707 autosampler, a 1515 isocratic HPLC pump, and a 2414 refractive index detector. Two styragel columns (Polymer Laboratories; 5 μ m Mix-C), which were kept in a column heater at 35 $^{\circ}$ C, were used for separation. The columns were calibrated with polystyrene standards (Varian). Ultraviolet–visible (UV–vis) absorption spectra were recorded on a Shimadzu UV-2401 PC spectrometer over a wavelength range of 240–800 nm. Fluorescence emission spectra were obtained on a Varian Cary Eclipse fluorimeter. Atomic force microscopy (AFM) measurements were performed on an Asylum MFP3D AFM instrument operated under tapping mode. Images were obtained directly from corresponding OPV devices. Optical micrographs were taken on a Carl Zeiss Axio Imager 2 microscope at a 400 \times magnification. Transmission electron microscopy (TEM) images were taken on a JEOL 2010 high resolution TEM operated at 200 kV. Samples were prepared by drop-casting corresponding blend solutions onto carbon coated copper grids (200 mesh, SPI Supplies) atop a filter paper and dried under vacuum. Wide-angle and small-angle X-ray scattering experiments were

performed at the X9 undulator-based beamline at the National Synchrotron Light Source (NSLS). An incident X-ray beam of energy 13.5 keV (wavelength = 0.0918 nm) was collimated using a two-slit system and focused to a beam 50 μ m tall by 100 μ m wide at the sample position using a KB mirror system. Grazing-incidence experiments were performed over a range of incidence angles, both below and above the film-vacuum critical angle. Two-dimensional scattering images were measured in the small-angle (GISAXS) using a charged-coupled device (CCD) detectors positioned at 5.330 m from the sample. Data in the wide-angle (GIWAXS) were recorded using a CCD detector 263 mm from the sample. Data conversion to q -space was accomplished using Silver Behenate powder as a standard. The orientation distribution of the crystalline P3HT was assessed using previously established methods.^{59–62} Briefly, the intensity along the polymer (100) lamellar peak ($q \sim 0.39 \text{ \AA}^{-1}$) was integrated as a function of the angle (χ) with respect to the q_z axis. The full peak width was integrated, with the background at each χ subtracted by measuring the intensity just outside the peak region. The χ scale was corrected to account for the intersection of the Ewald with reciprocal space.⁶² To convert from scattering intensity to a measure of amount of material, we need to account for the finite intersection of the Ewald sphere with the three-dimensional reciprocal space. Since the films studied here are in-plane powders (symmetry about the q_z axis), we adjust the scattering intensity by $\sin(\chi)$. We decompose the corrected curve's integrated intensity into three groups, in order to estimate the relative amounts of isotropic (the subset of material exhibiting a 3D isotropic orientation distribution), edge-on, and face-on material. Isotropically ordered polymer produces a ring of uniform intensity in the original scattering data (and thus a curve that goes as $\sin(\chi)$ in the corrected data). The intensity above this baseline is divided into edge-on ($\chi < 45^{\circ}$) and face-on ($\chi > 45^{\circ}$), where "edge-on" refers to a polymer with the lamellar stacking oriented roughly vertically (and thus the (100) peak appears near the q_z axis), and "face-on" refers to a polymer with the thiophene ring roughly parallel with the substrate plane (and thus the (100) peak appears near the q_r axis). Although the use of a cutoff at 45° in principle includes material oriented with a substantial skew (with respect to q_z or q_r), in practice we observed essentially bimodal populations (after removal of the isotropic component) peaked near the q_z or q_r axes. In order to provide more details regarding our orientational analysis, we have added the intensity integrations along the P3HT (100) lamellar peak (pole figures) to the Supporting Information. The measured detector intensity plots are included in Figure S9, and the "corrected" curves that account for the in-plane symmetry of the samples are included in Figure S10.

2.2. General Methods for NF Preparation. In a dry vial was added 5 mg of polymer (**P1** or P3HT) and 0.5 mL of anhydrous chlorobenzene. The solution was heated with stirring at 100 $^{\circ}$ C for 1 h inside a nitrogen glovebox and then stirred at room temperature (r.t) for 1 h. Acetone of predetermined volume was then added dropwise via a microsyringe. The solution was then kept stirring at room temperature for predetermined periods of time before analysis. For preformed polymer/PCBM composite NF blends: the polymer NF solution was transferred to another vial containing 2 mg of PCBM powder, and the solution was kept stirring at r.t. for 12 h before analysis and device fabrication. For in situ formed polymer/PCBM composite NF blends: identical procedure to that for pure polymer NF formation except an additional 2 mg of PCBM was added at the beginning of sample preparation.

2.3. OPV Fabrication and Testing. A conventional structure of ITO/MoO₃/active layer/Al was adopted for the OPV devices studied. Devices were fabricated according to the following procedures. Unpatterned ITO-coated glass substrates (China Shenzhen Southern Glass Display, Ltd., 8 Ω/\square) were cleaned by ultrasonication sequentially in detergent, DI water, acetone, and isopropyl alcohol, each for 15 min. These ITO-coated glass substrates were further treated by UV-ozone (PSD Series, Novascan) for 45 min before being transferred to a nitrogen glovebox (Innovative Technology, model PL-He-4GB-1800, O₂ < 0.1 ppm, H₂O < 0.1 ppm) for MoO₃ deposition. MoO₃ (10 nm) was deposited using an Angstrom Engineering \AA mod system equipped with four thermal resistive deposition sources at a

base vacuum level $<7 \times 10^{-8}$ Torr. Polymer/PCBM blend solutions were spun cast on top of the MoO_3 layer at 400 rpm for 30 s to give a thin film thickness of ca. 100 nm as measured by profilometry. Al (100 nm) was thermally evaporated through patterned shadow masks. The size of the solar cells is ca. 3.14 mm^2 . Current–voltage (I – V) characteristics were measured by a Keithley 2400 source-measuring unit under simulated AM 1.5G irradiation (100 mW/cm^2) generated by a Xe arc-lamp based Newport 67005 150W solar simulator equipped with an AM 1.5G filter (unmasked). The light intensity was calibrated by a Newport thermopile detector (model 818P-010-12) equipped with a Newport 1916-C Optical Power Meter.

3. RESULTS AND DISCUSSION

3.1. Solution Studies. Detailed synthesis and characterization of **P1** ($M_n = 27.2 \text{ kDa}$, $PDI = 1.6$; size exclusion chromatography against polystyrene standards, 35°C , CHCl_3 eluent, 1 mL/min) have been reported previously.^{57,58} **P1** has a block length ratio between unfunctionalized and functionalized segments of ca. 6:1 (Scheme 1). The homo-P3HT block is designed to be relatively long in order to ensure sufficient driving force for self-assembly into NFs. The IOA functional group concentration is thus calculated to be ca. 7%. In order to confirm the existence of noncovalent interactions between IOA groups and PCBM, fluorescence of **P1** in dilute chlorobenzene solution (10^{-5} M repeat unit) was monitored with gradual addition of PCBM, and the results are summarized in Figure S1(a). The fluorescence intensity of **P1** was quenched by ca. 16% with the addition of 2 equiv (per repeat unit of **P1**) of PCBM. The Stern–Volmer plot showed a two-step transition. A sharp rise having a large Stern–Volmer constant (K_{SV}) of $5.1 \times 10^{-4} \text{ M}^{-1}$ was observed initially up to ca. 7% PCBM addition, the exact amount of fullerenes needed to form one-on-one complexes with all the IOA moieties on **P1**. After this point, a 10-fold smaller K_{SV} of $4.3 \times 10^{-3} \text{ M}^{-1}$ was observed. Under identical conditions, decrease of fluorescence intensity of P3HT homopolymers (synthesized in-house, $M_n = 31.2 \text{ kDa}$, $PDI = 1.04$), which is not capable of directional noncovalent interactions with PCBM, was less than 7% as shown in Figure S1(b). Only a straight Stern–Volmer plot having a K_{SV} of $4.5 \times 10^{-3} \text{ M}^{-1}$ was obtained for P3HT, comparable to the second step in that of **P1**. These observations suggest strong and directional noncovalent interactions between IOA and PCBM moieties. Thus, a 7 mol % of PCBM, which corresponds to a polymer/PCBM weight ratio of 10/4, was used throughout the current studies.

Formation of NFs from **P1** and **P1**/PCBM mixtures was first studied by UV–vis absorption measurements as shown in Figure 1. Commonly applied “whisker” methods, i.e. slow crystallization of P3ATs in a single marginal solvent,^{32,34–36} require relatively low concentrations of polymer, which makes device fabrication from such dilute solutions difficult. We thus undertook the “mixed solvent” approach^{49,63,64} by adding acetone, a nonsolvent for P3HT but a good one for IOA moieties, into chlorobenzene solutions. The initial concentration of **P1** was set to 10 mg/mL , which is commonly used in conventional P3HT/PCBM BHJ devices. Different amounts of acetone were then added into a set of such **P1** solutions and aged at room temperature for 14 h before dilution for absorption measurements.⁶⁵ As shown in Figure 1A, with an increasing amount of acetone, the absorption profiles red shift and the vibronic features at 514, 522, and 603 nm became more pronounced, indicating the formation of more ordered aggregates.^{66,67} Beyond an acetone/chlorobenzene volume ratio of 1/5, polymer precipitation was visually detectable

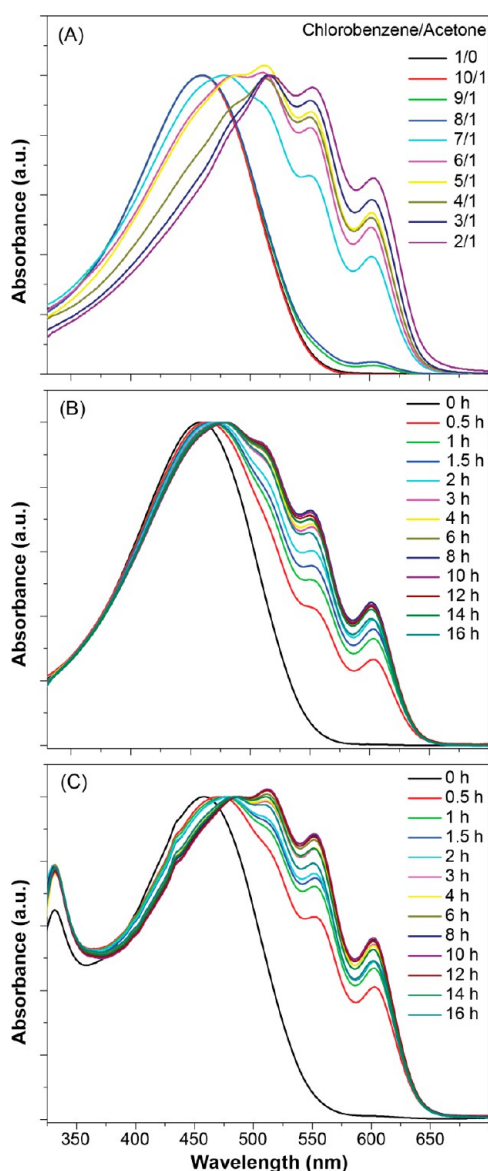


Figure 1. UV–vis absorption spectra of (A) **P1** in chlorobenzene (10 mg/mL) with addition of various amounts of acetone (vol./vol.); (B) **P1** in chlorobenzene (10 mg/mL) at different time intervals upon addition of acetone (chlorobenzene/acetone: 5/1, vol./vol.); and (C) **P1** (10 mg/mL) and PCBM (4 mg/mL) in chlorobenzene at different time intervals upon addition of acetone (chlorobenzene/acetone: 5/1, vol./vol.). All spectra were taken by diluting the corresponding original solutions with identical mixed solvents to a final **P1** concentration of 0.025 mg/mL .

despite the continually enhanced vibronic features in absorption spectra. Such precipitation could potentially complicate the following self-assembly studies and significantly affect film formation during OPV device fabrication. Thus, the acetone/chlorobenzene mixed solvents at a 1/5 volume ratio were chosen throughout the current study.

We then studied aggregation kinetics of **P1** with and without PCBM in the mixed solvents by monitoring their absorption spectra with time, as shown in Figure 1B and 1C, respectively. Upon addition of acetone, the color of **P1** solution changed gradually from red-orange to dark brown without the appearance of any visible aggregates. Due to high optical density of the original solution, a sample was withdrawn at

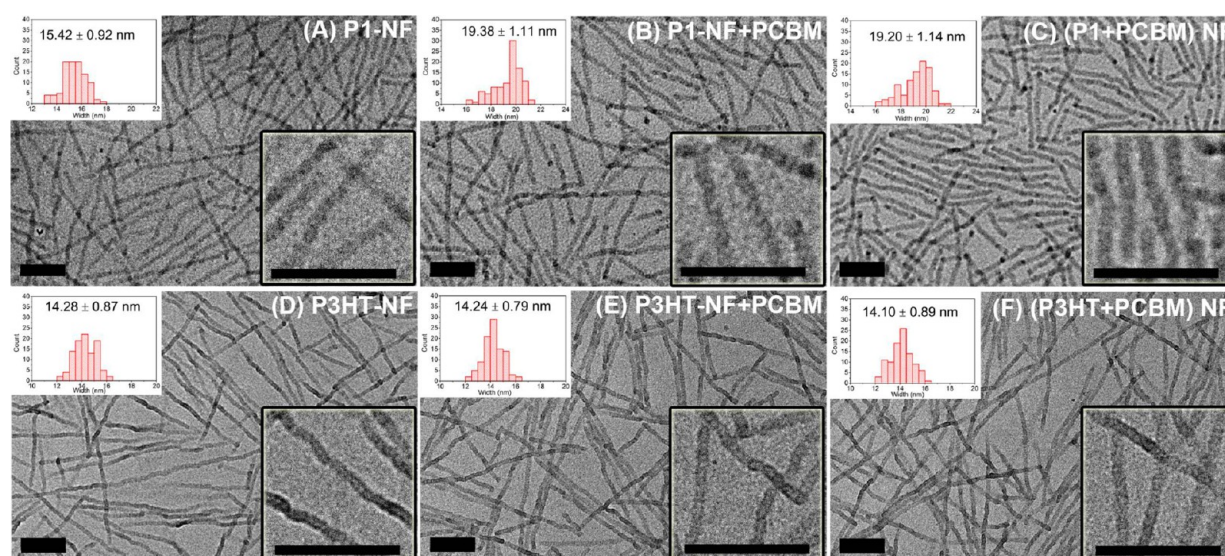


Figure 2. Transmission electron microscopy (TEM) images of (A) P1 nanofibers (NFs); (B) preformed P1 NFs with the addition of PCBM (40 wt %); (C) NFs in situ formed from the P1/PCBM (10/4, wt./wt.) mixture solution; (D) P3HT NFs; (E) preformed P3HT NFs with the addition of PCBM (40 wt %); and (F) NFs in situ formed from the P3HT/PCBM (10/4, wt./wt.) mixture solution. NFs are formed by addition of acetone to chlorobenzene solutions (1/5, vol./vol.) of polymer or polymer/PCBM mixtures (10 mg/mL of polymer in chlorobenzene) and aged for 12 h. Top left inserts: distributions of fiber widths sampled from 100 individual NFs. Bottom right inserts: magnified images. Scale bars in all: 200 nm.

predetermined time intervals and diluted with identical mixed solvents 400 times for absorption measurements. The color of the diluted solutions changed gradually from yellow to brownish red as shown in Figure S2. In the absorption spectra (Figure 1B), the vibronic peaks increase in relative intensity up to 12 h aging time due to continuous growth of polymer NFs,⁶⁸ beyond which a slight decrease was observed. We do not fully understand the reason for such behavior at present. It is possible that frequent sampling led to slow evaporation of the more volatile acetone solvent, resulting in better solvation for P1. This change in solvents composition likely explains the unexpected more pronounced vibronic features in the 5/1 composition absorption profile in Figure 1A when compared with the 14 h aging trace in Figure 1B. Both conditions should supposedly lead to similar P1 nanostructures and absorption profiles, but in the former case the solution was kept tightly closed throughout the entire duration of experiment and thus no acetone evaporation was possible. As a result, seemingly stronger aggregation behavior was observed. Similar kinetics was observed for the P1/PCBM (10/4 by weight) mixture solution (Figure 1C). An aging time of 12 h was again found to be optimal to achieve the highest ordered aggregates with the most enhanced vibronic absorption features, beyond which a decrease in relative intensity was observed. Thus, the 12 h aging time was chosen for all NF formation studies in this account. Interestingly when comparing Figure 1B with 1C, the vibronic features are significantly more pronounced in aggregates formed from the P1/PCBM mixture solution than those in the P1 solution, indicating more ordered aggregates of P1 in the presence of PCBM. This can likely be explained by noncovalent interactions existing among IOA and PCBM moieties. In the absence of PCBM, inter- and intrachain interactions between IOA groups on P1 can potentially disrupt ordered packing of polymer chains to some extent. With the addition of 40 wt % PCBM, all the IOA moieties are expectedly occupied by fullerene molecules, which leads to decreased interaction among individual P1 chains and thus enhanced tendency for packing into more ordered structures. Such

observations support the relatively strong noncovalent interactions between IOA groups and PCBM molecules.

The P1 related nanostructures were directly visualized by transmission electron microscopy (TEM), and the results are summarized in Figure 2. For comparison, TEM images of P3HT NFs formed under identical conditions are also included in Figure 2, and their corresponding absorption spectra are shown in Figure S3. Both P1 and P3HT formed uniform NFs having lengths up to several micrometers. The P3HT NFs have an average width of ca. 14.3 nm that is very close to the literature reported values for high molecular weight regioregular P3HT NFs (Figure 2D).³⁶ On the other hand, the average width of P1 NFs is slightly larger at ca. 15.4 nm (Figure 2A). Likely, addition of acetone induces typical NF formation of the P3HT block of P1, while the IOA functionalized block remains more solubilized and stretches away from the more compact P3HT NFs. Indeed, addition of 40 wt % PCBM into the preformed P1 NF solution led to little change in overall NF shapes but significant increase in fiber widths to an average of ca. 19.4 nm (Figure 2B). Such an increase in fiber widths can be reasonably explained by attachment of PCBM molecules onto peripherals of P1 NFs due to noncovalent interactions with IOA moieties. On the other hand, addition of 40 wt % PCBM into preformed P3HT NFs caused no detectable changes in both fiber appearance and widths (Figure 2E), since no strong or specific interactions exist between P3HT homopolymers and PCBM molecules. Similar behaviors were observed in composite NFs formed in situ from polymer/PCBM mixture solutions. As shown in Figure 2C, NFs formed from P1/PCBM (10/4, wt./wt.) mixture solutions have very similar widths with those from preformed solutions and only somewhat reduced fiber lengths. This indicates similar formation mechanisms and NF structures in both cases. Again, NFs formed from P3HT/PCBM (10/4, wt./wt.) mixture solutions have identical geometrical parameters (Figure 2F) with pure P3HT NFs as well as those having PCBM added subsequently. These TEM images directly confirm the ability to form tunable CP/fullerene composite nanostructures through cooperative noncovalent

Table 1. Optimized OPV Device Performance of P1 or P3HT/PCBM (10/4, wt./wt.) under Different Conditions^a

	conditions	PCE (%) ^b	J_{SC} (mA/cm ²) ^c	V_{OC} (V) ^d	FF ^e
P1/PCBM	preformed NFs	4.17 ± 0.15	11.23 ± 0.53	0.62 ± 0.00	0.60 ± 0.01
	in situ formed NFs	3.52 ± 0.20	11.62 ± 0.51	0.61 ± 0.01	0.50 ± 0.01
	BHJ	3.00 ± 0.08	8.82 ± 0.28	0.65 ± 0.01	0.52 ± 0.00
P3HT/PCBM	preformed NFs	3.32 ± 0.21	9.93 ± 0.53	0.57 ± 0.01	0.59 ± 0.01
	in situ formed NFs	3.11 ± 0.21	10.63 ± 0.52	0.52 ± 0.01	0.56 ± 0.01
	BHJ	2.85 ± 0.07	9.20 ± 0.39	0.59 ± 0.01	0.52 ± 0.01

^aSpin-cast from chlorobenzene solutions (10 mg/mL polymer concentration) at 400 rpm for 30 s and thermally annealed at 150 °C for 15 min. All values are reported as average from five individual cells. ^bPower conversion efficiency under simulated 100 mW/cm² white light irradiation. ^cShort circuit current. ^dOpen circuit voltage. ^eFill factor.

interactions including P3HT crystallization, block copolymer self-assembly, and hydrogen bonding interactions.

3.2. OPV Device Performance. OPV devices were fabricated from both preformed and in situ formed P1/PCBM and P3HT/PCBM composite NF solutions with a polymer to fullerene weight ratio of 10:4. For comparison, conventional BHJ devices were fabricated from polymer/PCBM mixture (10/4 wt./wt.) solutions in pure chlorobenzene. All devices adopted conventional structures: ITO glass/MoO₃ (10 nm)/active layer (100 nm)/Al (100 nm). Thermally evaporated MoO₃ was used as the anode interfacial layer instead of the commonly applied PEDOT:PSS in order to avoid disruption of desired hydrogen bonding interactions by the highly acidic nature of the later. All devices were optimized by thermal annealing at 150 °C for 15 min, and cell performances are summarized in Table 1.

Despite the relatively low contents of PCBM, all devices showed decent performance, and the best power conversion efficiencies (PCEs) of 4.17 ± 0.15% were observed in devices employing preformed P1/PCBM composite NFs. To the best of our knowledge, this is the highest PCE displayed in single junction OPV devices employing P3HT and a PCBM content as low as 28 wt %. This low content of PCBM seems to be sufficient to generate percolating pathways for both electron donors and acceptors for efficient charge generation and collection in these composite NF films, which is hard to achieve through simple blending of the two materials. Compared with BHJ counterparts, devices made from either P1 or P3HT composite NFs respectively showed higher PCEs, originating mostly from higher short circuit current (J_{SC}). This increase in J_{SC} is likely due to controlled and more favorable confinement of CP domains, via NF formation, to sizes comparable to exciton diffusion lengths. Higher J_{SC} values were also observed in devices employing P1 composite NFs than those using P3HT NFs. Since both polymer NFs have similar widths as confirmed by TEM measurements, such differences in current density can likely be explained by more efficient charge dissociation at the P1 NF/PCBM interfaces. Due to the noncovalent interactions, more PCBM molecules are attracted to and closely associated with P1 NFs than with P3HT NFs, which expectedly leads to enhanced charge separation efficiencies in devices employing P1 NFs. Interestingly, devices employing P1 gave higher open circuit voltage (V_{OC}) than those made from P3HT. Deeper-lying HOMO energy levels and thus larger V_{OC} have been commonly found in OPV devices employing less crystalline CPs.⁶⁹ Presumably, stronger interactions between P1 and PCBM disturb close packing of the P3HT segments, making the P1 NF domains less crystalline. Such effects are discussed further in later sections.

Formation of NFs and noncovalent interactions between P1 and PCBM can potentially prevent or decelerate macroscopic phase separation and thus improve device thermal stability. The above optimized devices were then subjected to thermal annealing at 110 °C up to 112 h and tested at predetermined time intervals. Results of the aging tests are summarized in Figure 3 and Figures S4 and S5.

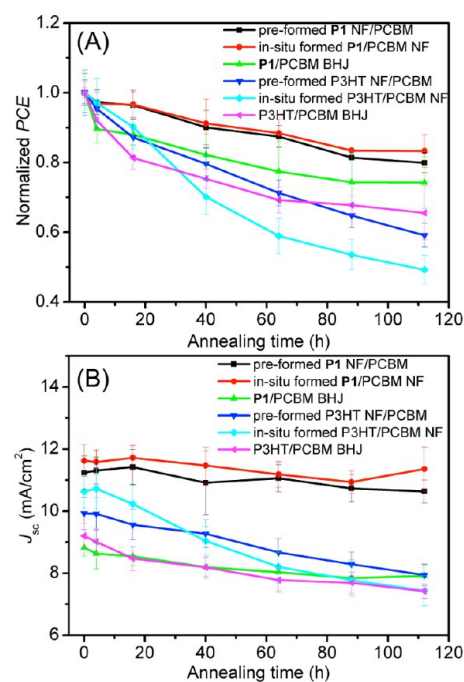


Figure 3. Thermal stability tests of devices employing P1/PCBM (10/4, wt./wt.) and P3HT/PCBM (10/4, wt./wt.) under different blending conditions. Devices were thermally annealed at 110 °C under nitrogen for various times: (A) PCE against annealing time and (B) J_{SC} against annealing time.

Devices made from P1/PCBM composite NFs, either preformed or in situ formed, showed the highest stability with over 80% PCE retention after aging (Figure 3A). High stability of these devices is derived from relatively stable J_{SC} (Figure 3B) and V_{OC} (Figure S4A). The slight decreases in PCEs are mostly caused by slight droppings in FFs as seen in Figure S4B and Figure S5. P1/PCBM BHJ devices are less stable with slightly less than 80% PCE retention after aging but still outperform all devices made from P3HT. Small decreases in both J_{SC} and FF are responsible for the observed performance deterioration. On the other hand, devices made from both preformed and in situ formed P3HT NFs displayed the worst thermal stability, especially the later giving at least

50% reduction in *PCE* after aging. A slight drop in V_{OC} and significant decreases in J_{SC} and *FF* all contribute to degradation of both types of devices. Interestingly, the P3HT/PCBM BHJ devices showed somewhat higher thermal stability than those employing P3HT NFs. As seen in Figure S5, all three device parameters experience decline to a less extent in the P3HT BHJ devices relative to those using P3HT NFs.

3.3. Morphology Studies. V_{OC} in all devices was shown to be relatively thermally stable, indicating a small disturbance of energetics at organic/organic and organic/electrode interfaces. Thus, the decreases in J_{SC} and *FF* largely contributing to device degradation are most likely caused by morphology instability and possible macrophase separation. The existence of a noncovalent interaction between **P1** and PCBM can potentially slow down thermally induced macrophase separation and thus leads to enhanced morphological stability.

Phase separations in these devices were first studied by optical microscopy, and representative micrographs are shown in Figure 4. The microscope was set to 400 \times magnification, and

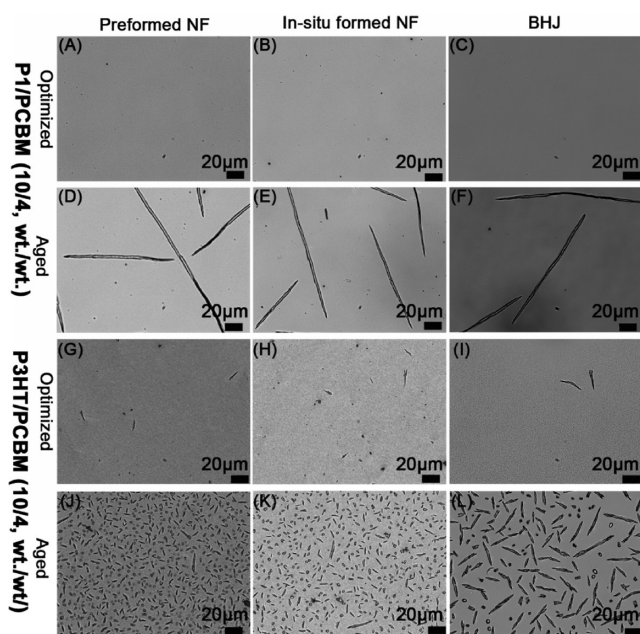


Figure 4. Optical micrographs of optimized (150 °C, 15 min, A–C and G–I) and aged (110 °C, 112 h, D–F and J–L) devices employing preformed **P1**/PCBM composite NFs (A and D), in situ formed **P1**/PCBM composite NFs (B and E), **P1**/PCBM BHJ blends (C and F), preformed P3HT NF/PCBM (G and J), in situ formed P3HT/PCBM NFs (H and K), and P3HT/PCBM BHJ blends (I and L). Polymer/fullerene weight ratio is 10/4 in all devices. Scale bars in all: 20 μ m.

PCBM crystallites appeared as darker areas in these pictures. Upon optimization (thermal annealing at 150 °C for 15 min), very few PCBM crystals can be observed in devices containing **P1**, and sparsely located PCBM crystallites are clearly seen in those employing P3HT. After aging tests (thermal annealing at 110 °C for 112 h), a few unusually large needle-shaped PCBM crystals having lengths up to several hundred micrometers can be observed in devices using **P1**. Formation of such large crystals is likely due to very slow crystallization processes of PCBM molecules that in turn reflect more stabilized morphology.

On the other hand, much shorter and significantly denser PCBM crystals are found in devices employing P3HT,

indicating faster PCBM aggregation processes and more pronounced macrophase separation. Noticeably in Figure 4L, PCBM crystals are relatively larger and less densely packed in P3HT/PCBM BHJ devices than in those using P3HT NFs (Figures 4J and 4K). This observation indicates slower PCBM crystallization and thus relatively more stable morphology in the P3HT BHJ devices, which is consistent with device stability data discussed in the previous section. Presumably in the P3HT NF devices, formation of interconnected P3HT NFs also leads to interpenetrating voids that are filled with PCBM molecules. Upon thermal annealing, these PCBM molecules can more easily find each other, aggregate, and emerge between polymer NFs. Such spatial arrangement is less predominant in the BHJ devices, leading to slower PCBM crystallization kinetics. As for the devices employing **P1**, there exist noncovalent interactions between the polymer and fullerene molecules in both NF and BHJ devices, which effectively slows down PCBM aggregation as well as macrophase separation.

Detailed phase-separation and morphological features on the nanometer scale were probed using atomic force microscopy (AFM). Figure 5 compiles phase images of active layers of the OPV devices, and corresponding height images are included in Figure S6. Clear differences in topography are observable between devices containing P3HT and **P1**, as well as between devices employing NFs and BHJ blends. Distinctive, long, and straight P3HT NFs dominate as-cast devices employing both preformed (Figure 5j) and in situ formed (Figure 5m) NFs. Upon thermal optimization and aging, these NFs are still clearly observable but become slightly more curved, less obvious, and more closely packed. This phenomenon is consistent with large-scale phase separation and PCBM molecules aggregating out of the space between NFs and is thus in agreement with optical microscopy and stability tests. Integrity of these P3HT NFs remains largely undisturbed, indicating high thermal stability of the P3HT NFs. Figures 5p to 5r show typical P3HT/PCBM BHJ morphologies having short, irregular P3HT fibrils and reduced PCBM domain sizes upon extended thermal annealing. As a result, discrete P3HT NFs in solid state are more easily obtained by preforming the nanostructures in solutions before thin film deposition, and thermally annealing disordered polymer films is not likely to induce well-defined chain packing leading to long NFs. On the other hand, devices employing **P1** composite NFs, either preformed or in situ formed, showed very similar morphology in as-cast, optimized, and aged films, confirming the higher stability of active layer morphologies. Compared with P3HT NF devices, straight and long NFs, although detectable, are much less apparent in devices using **P1** NFs. Noncovalent coating of PCBM molecules likely interconnects **P1** NFs in the solid state, distorting the NFs and making the fiber boundaries less discernible by AFM. Similarly in the **P1**/PCBM BHJ devices, only irregular polymer fibrils can be observed, and very similar images are obtained for both optimized and aged devices, indicating good thermal stability and consistent with device stability tests.

In order to gain a deeper insight into the effectiveness of our composite NF strategy on morphology controllability, we performed both grazing-incidence wide-angle X-ray scattering (GIWAXS) and grazing-incidence small-angle X-ray scattering (GISAXS) measurements on thin films of polymer NFs, polymer/PCBM composite NFs, and polymer/PCBM BHJ blends. The results are summarized in Figures 6 and 7, Table 2, and Figures S7–S10.

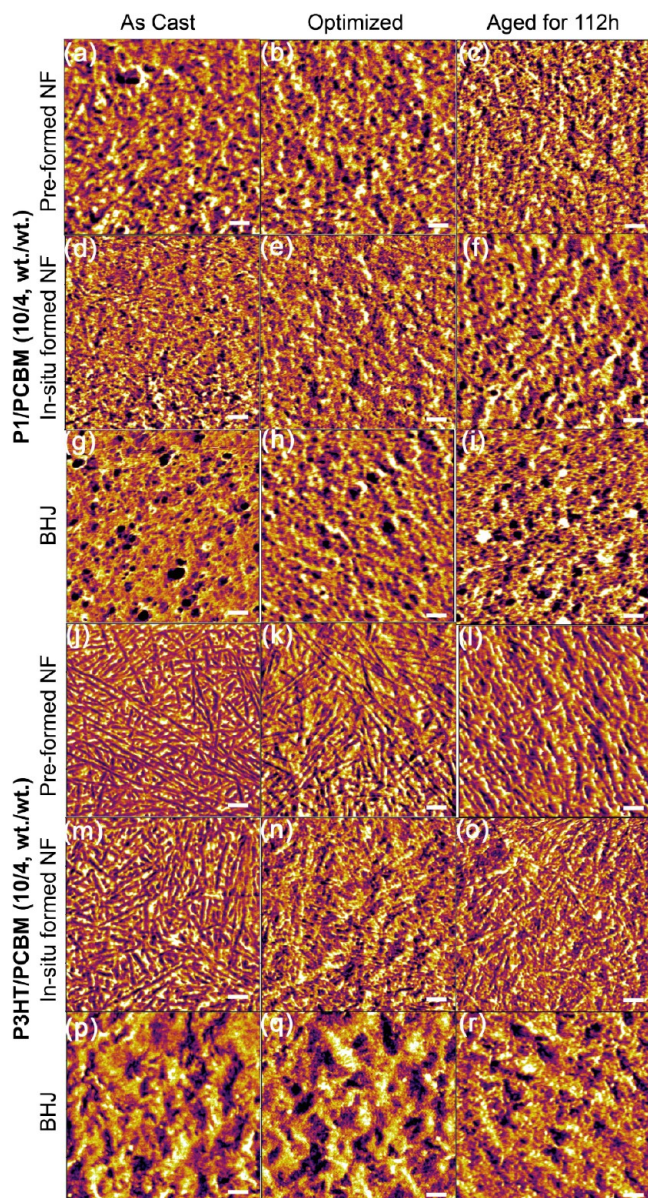


Figure 5. Atomic force microscopy (AFM) phase images ($2 \mu\text{m} \times 2 \mu\text{m}$) of as-cast (left column), optimized (150°C , 15 min, middle column) and aged (110°C , 112 h, right column) devices employing preformed P1/PCBM composite NFs (a–c), in situ formed P1/PCBM composite NFs (d–f), P1/PCBM BHJ blends (g–i), preformed P3HT NF/PCBM (j–l), in situ formed P3HT/PCBM NFs (m–o), and P3HT/PCBM BHJ blends (p–r). Polymer/fullerene weight ratio is 10/4 in all devices. Scale bars in all: 200 nm.

GIWAXS enables probing of the molecular-scale packing of the components and is particularly sensitive to the efficient organization of P3HT (or P1) in two orthogonal directions: the π - π stacking of the aromatic thiophene rings giving rise to scattering peaks at q -values of ca. 1.64 \AA^{-1} , and the lamellar stacking that results from the disordered alkyl side-chains giving rise to (100), (200), and (300) peaks at q -values of ca. 0.39 \AA^{-1} , 0.79 \AA^{-1} , and 1.18 \AA^{-1} , respectively. We note that the third orthogonal direction (along the polymer backbone) does not give rise to a well-defined GIWAXS peak. Additionally, PCBM crystallites give rise to GIWAXS signals at q -values of ca. 1.40 \AA^{-1} . The intensity along the scattering rings can also be used to quantify the orientation distribution of the material and thus

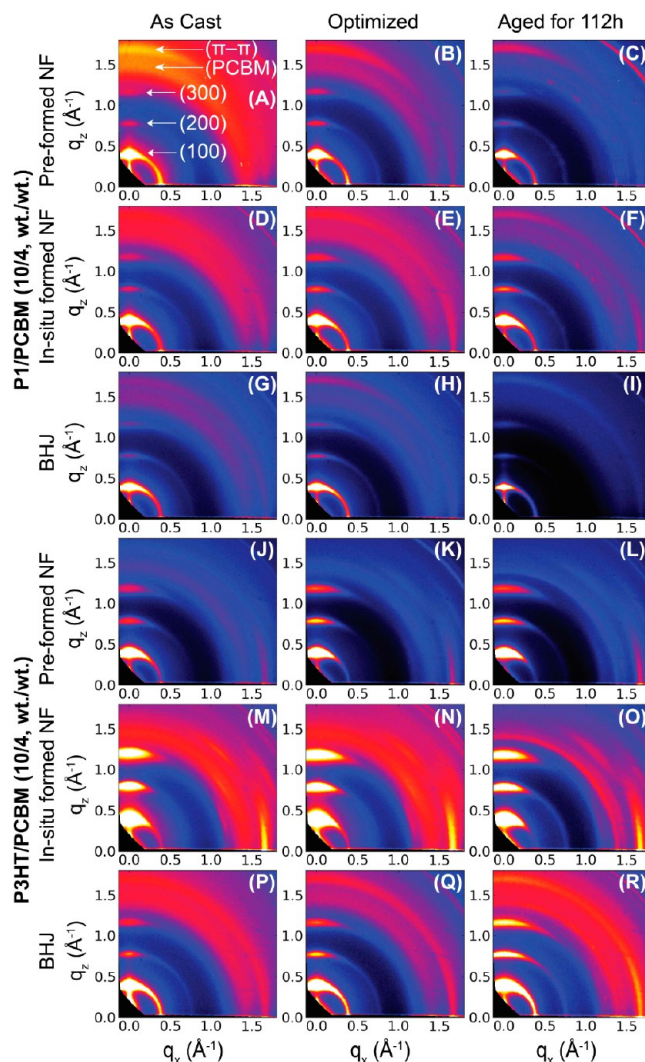


Figure 6. Grazing-incidence wide-angle X-ray scattering (GIWAXS) profiles of as-cast (left column), optimized (150°C , 15 min, middle column) and aged (110°C , 112 h, right column) devices employing preformed P1/PCBM composite NFs (a to c), in situ formed P1/PCBM composite NFs (d to f), P1/PCBM BHJ blends (g to i), preformed P3HT NF/PCBM (j to l), in situ formed P3HT/PCBM NFs (m to o), and P3HT/PCBM BHJ blends (p to r). Polymer/fullerene weight ratio is 10/4 in all devices. The presented images are for a grazing-incident angle of 0.12° (other angles measured gave similar results). Color scales in all images are identical.

the fractions of materials oriented in different directions.^{59,60} We observed strong scattering peaks for all of the processing conditions, indicating good ordering (crystallization) of the P3HT (or P1) phase. However, there are notable differences between the different materials and processing conditions. Thin films containing P3HT NFs generally gave stronger and more defined higher order scattering peaks than those containing P1 NFs under comparable conditions as shown in Figures 6 and S7, indicating higher crystallinity in the P3HT NFs. This is consistent with the higher V_{OC} observed in OPV devices employing P1 NFs due to the less crystalline nature. The P3HT/PCBM samples all exhibit the “edge-on” orientation typically observed for these materials, wherein the side-chains interact with the substrate interface, giving rise to the out-of-plane lamellar peaks, and corresponding in-plane π - π peaks. This should be contrasted with the “face-on” orientation, which

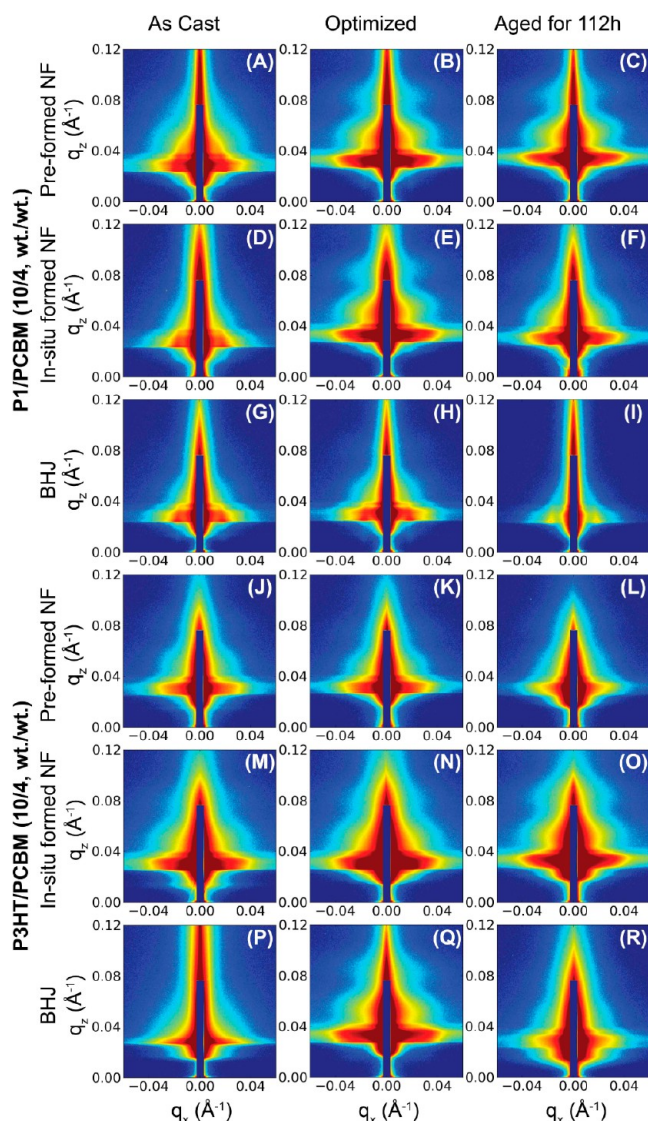


Figure 7. Grazing-incidence small-angle X-ray scattering (GISAXS) profiles of as-cast (left column), optimized (150 °C, 15 min, middle column), and aged (110 °C, 112 h, right column) devices employing preformed P1/PCBM composite NFs (a to c), in situ formed P1/PCBM composite NFs (d to f), P1/PCBM BHJ blends (g to i), preformed P3HT NF/PCBM (j to l), in situ formed P3HT/PCBM NFs (m to o), and P3HT/PCBM BHJ blends (p to r). Polymer/fullerene weight ratio is 10/4 in all devices. The presented images are for a grazing-incident angle of 0.12° (other angles measured gave similar results). Color scales in all images are identical.

has the aromatic rings stacked along the film normal instead and which is expected to give rise to higher out-of-plane hole mobility and thus more suitable for OPV operations.

Whereas the P3HT/PCBM samples all exhibit predominantly edge-on orientation (with <7% face-on orientation), as summarized in Table 2, the P1/PCBM materials instead break this deleterious orientational effect. For instance, the P3HT/PCBM preformed NFs, after aging, exhibited 94% edge-on orientation. By comparison, the corresponding preformed P1/PCBM composite NFs exhibited only 36% edge-on orientation (and 11% face-on plus 52% of a uniformly distributed (isotropic) material). This reorientation of material can be seen as a bimodal distribution of scattering intensity along the P1 lamellar scattering peaks. It is possible that the P3HT/

PCBM NFs are efficiently oriented by the substrate/film and film/air interfacial wetting preferences of the P3HT alkyl side-chains. The strong interactions between P1 and PCBM modify this interfacial interaction and allow the composite NFs to achieve greater orientational freedom. This modified orientation distribution is likely to contribute to improved J_{SC} and thus enhanced solar cell performance.

Unsurprisingly, annealing improves order for all the materials studied, with higher-order peaks becoming better defined. Interestingly, however, there is some suggestion that the P1/PCBM composite NFs cause the PCBM phase to crystallize, as evidenced by the appearance of textured scattering rings at the distance corresponding to PCBM packing. This was only observed for aged samples of P1/PCBM composite NFs, indicating that NFs of this material cause some structuring of surrounding material (even while preventing larger-scale phase-separation). The aged materials (annealing for 112 h) exhibit some reorientation of the material. Notably, this reorientation was less pronounced for P1 than for P3HT composites, again suggesting that the strong interactions between P1 and PCBM stabilize the morphology.

The GISAXS data probes nanoscale order and confirms the AFM observations previously described. Although weakly observed in BHJ films, all the NF samples exhibit a strong broad undulation of scattering intensity along the vertical direction (Figures 7 and S7), whose spacing (0.035 Å⁻¹) is consistent with the form-factor for the cylindrical cross-section of the NFs (ca. 18 nm diameter). In the P1/PCBM composite NFs as well as BHJ thin films, a distinct in-plane GISAXS peak is observed, which suggests a well-defined nanoscale ordering of the two heterojunction materials. Figure S8 summarizes 1D curves from the SAXS data by integrations through the scattering peak in the purely in-plane direction, which measures the in-plane size-scale of the ordering. In particular, a well-defined spacing of 33–35 nm with a corresponding grain-size of ca. 200 nm (measured from the peak width) exists in all the P1 samples and appears to be robust with respect to annealing. On the other hand, no such ordering could be observed in all thin films containing P3HT and those of P1 NF alone. Although in the AFM measurements, only P3HT gave discrete NFs having high aspect ratios, the GISAXS results are indicative of well-defined packing of the NFs themselves over remarkably long distances (ca. 6 NF/PCBM repeats) only in the cases of P1/PCBM composite NFs. The observed GISAXS peaks are presumably caused by preferred packing distance for P1 NFs due to strongly associated PCBM molecules segregating between them. Such effects are absent in P1 alone NF films as well as films containing P3HT/PCBM, wherein the heterojunctions are not well structured and thus no scattering peaks could be observed. These results suggest that the strong interactions between P1 and PCBM can indeed lead to the formation of a well-defined and highly stable nanoscale morphology.

4. CONCLUSION

In summary, we have developed a modular approach for achieving stable and controllable bulk heterojunction nanomorphology toward more efficient and thermally robust OPV devices. By building in noncovalent interactions between one segment of a conjugated block copolymer and fullerene derivatives, well-defined composite NFs are obtained through self-assembly in solution. Such supramolecular nanostructures lead to more device favorable polymer orientation, enhanced

Table 2. Summary of Grazing Incidence X-ray Scattering Results^a

conditions	GIWAXS (as cast/optimized/aged) ^b			GISAXS (as cast/optimized/aged) ^c		
	face-on (%)	edge-on (%)	isotropic (%)	d-spacing (nm)	grain size (nm)	
P1/PCBM	P1 only NFs	8/5/4	67/81/68	25/14/27	n.o. ^e	n.o. ^e
	preformed NFs	11/15/11	27/39/36	63/46/52	33/34/n.c. ^d	243/190/n.c. ^d
	in situ formed NFs	3/2/2	51/58/68	47/41/30	35/35/34	199/179/209
	BHJ	7/2/4	48/44/41	45/54/55	35/35/35	196/194/201
P3HT/PCBM	P3HT only NFs	2/3/1	97/92/98	2/5/1	n.o. ^e	n.o. ^e
	preformed NFs	5/3/3	75/90/94	19/7/3	n.o. ^e	n.o. ^e
	in situ formed NFs	2/2/1	93/94/96	5/4/2	n.o. ^e	n.o. ^e
	BHJ	6/3/6	44/56/70	50/41/24	n.o. ^e	n.o. ^e

^aThin films were deposited using identical conditions as that applied in OPV device fabrication. Optimized: 150 °C, 15 min; aged: 110 °C, 112 h. ^bGrazing-incidence wide-angle X-ray scattering. Percentages of different polymer orientations are estimated by integration the intensity along the scattering rings. ^cGrazing-incidence small-angle X-ray scattering. Grain size estimated from the peak width (Scherrer analysis), after accounting for instrumental resolution. ^dNot calculable. ^eNot observed.

morphology stability, and better defined and controllable morphologies. Our strategy opens up new possibilities in supramolecular chemistry and adds a promising tool for precision morphology engineering that can potentially lead to better performing OPVs, when extended to more efficient materials systems such as low bandgap conjugated polymers.

■ ASSOCIATED CONTENT

● Supporting Information

Fluorescence titration plot, photographs of P1 solutions upon aging, UV–vis absorption spectra of P3HT NF blended with PCBM, thermal stability test results, I–V curves under light for OPV performance and stability tests, AFM height images, X-ray scattering profiles of polymer NF only thin films, line-cut profiles for GISAXS measurements, raw and corrected integration plots along (100) lamellar peaks for GIWAXS measurements, and UV–vis absorption spectra of P1 NF solutions under various dilution conditions. This material is available free of charge via the Internet at <http://pubs.acs.org>.

■ AUTHOR INFORMATION

Corresponding Author

*E-mail: yangqin@unm.edu.

Notes

The authors declare no competing financial interest.

■ ACKNOWLEDGMENTS

The authors would like to acknowledge University of New Mexico for financial support for this research. Y.Q. acknowledges NSF Grant No. IIA-1301346 for financial support. K.Y. is supported by the Center for Functional Nanomaterials, which is funded by the U.S. Department of Energy, Office of Basic Energy Sciences under Contract No. DE-AC02-98CH10886.

■ REFERENCES

- (1) *Handbook of Conducting Polymers*, 3rd ed.; Skotheim, T. A., Reynolds, J. R., Eds.; CRC Press: Boca Raton, 2007.
- (2) Horowitz, G. *Adv. Mater.* **1998**, *10*, 365.
- (3) Facchetti, A. *Mater. Today* **2007**, *10*, 28.
- (4) Friend, R. H.; Gymer, R. W.; Holmes, A. B.; Burroughes, J. H.; Marks, R. N.; Taliani, C.; Bradley, D. D. C.; Dos Santos, D. A.; Brédas, J. L.; Lögdlund, M.; Salaneck, W. R. *Nature* **1999**, *397*, 121.
- (5) Yang, Y.; Chang, S.-C.; Bharathan, J.; Liu, J. *J. Mater. Sci.: Mater. Electron.* **2000**, *11*, 89.
- (6) Mortimer, R. J.; Dyer, A. L.; Reynolds, J. R. *Displays* **2006**, *27*, 2.
- (7) Beaujuge, P. M.; Reynolds, J. R. *Chem. Rev.* **2010**, *110*, 268.

- (8) Scott, J. C.; Bozano, L. D. *Adv. Mater.* **2007**, *19*, 1452.
- (9) Liu, C.-L.; Chen, W.-C. *Polym. Chem.* **2011**, *2*, 2169.
- (10) Thompson, B. C.; Fréchet, J. M. J. *Angew. Chem., Int. Ed.* **2008**, *47*, 58.
- (11) Dennler, G.; Scharber, M. C.; Brabec, C. J. *Adv. Mater.* **2009**, *21*, 1323.
- (12) Cheng, Y.-J.; Yang, S.-H.; Hsu, C.-S. *Chem. Rev.* **2009**, *109*, 5868.
- (13) Chen, J.; Cao, Y. *Acc. Chem. Res.* **2009**, *42*, 1709.
- (14) Brabec, C. J.; Gowrisanker, S.; Halls, J. M. J.; Laird, D.; Jia, S.; Williams, S. P. *Adv. Mater.* **2010**, *22*, 3839.
- (15) Nielsen, T. D.; Cruickshank, C.; Forged, S.; Thorsen, J.; Krebs, F. C. *Sol. Energy Mater. Sol. Cells* **2010**, *94*, 1553.
- (16) Jørgensen, M.; Carlé, J. E.; Søndergaard, R. R.; Lauritzen, M.; Dagnæs-Hansen, N. A.; Byskov, S. L.; Andersen, T. R.; Larsen-Olsen, T. T.; Böttiger, A. P. L.; Andreasen, B.; Fu, L.; Zuo, L.; Liu, Y.; Bundgaard, E.; Zhan, X.; Chen, H.; Krebs, F. C. *Sol. Energy Mater. Sol. Cells* **2013**, *119*, 84.
- (17) Chen, L.-M.; Hong, Z.; Li, G.; Yang, Y. *Adv. Mater.* **2009**, *21*, 1434.
- (18) Brabec, C. J.; Heeney, M.; McCulloch, I.; Nelson, J. *Chem. Soc. Rev.* **2011**, *40*, 1185.
- (19) Dang, M. T.; Hirsch, L.; Wantz, G.; Wuest, J. D. *Chem. Rev.* **2013**, *113*, 3734.
- (20) Liu, F.; Gu, Y.; Shen, X.; Ferdous, S.; Wang, H.-W.; Russell, T. P. *Prog. Polym. Sci.* **2013**, *38*, 1990.
- (21) Vandewal, K.; Himmelberger, S.; Salleo, A. *Macromolecules* **2013**, *46*, 6379.
- (22) You, J.; Dou, L.; Yoshimura, K.; Kato, T.; Ohya, K.; Moriarty, T.; Emery, K.; Chen, C.-C.; Gao, J.; Li, G.; Yang, Y. *Nat. Commun.* **2013**, *4*, 1446.
- (23) Liang, Y.; Xu, Z.; Xia, J.; Tsai, S.-T.; Wu, Y.; Li, G.; Ray, C.; Yu, L. *Adv. Energy Mater.* **2010**, *22*, E135.
- (24) Chu, T.-Y.; Lu, J.; Beaupré, S.; Zhang, Y.; Pouliot, J.-R.; Wakim, S.; Zhou, J.; Leclerc, M.; Li, Z.; Ding, J.; Tao, Y. *J. Am. Chem. Soc.* **2011**, *133*, 4250.
- (25) He, Z.; Zhong, C.; Su, S.; Xu, M.; Wu, H.; Cao, Y. *Nat. Photonics* **2012**, *6*, 591.
- (26) Jørgensen, M.; Norrman, K.; Krebs, F. C. *Sol. Energy Mater. Sol. Cells* **2008**, *92*, 686.
- (27) Conings, B.; Bertho, S.; Vandewal, K.; Sense, A.; D'Haen, J.; Manca, J.; Janssen, R. A. J. *Appl. Phys. Lett.* **2010**, *96*, 163301.
- (28) Vandenberg, J.; Conings, B.; Bertho, S.; Kesters, J.; Spoltore, D.; Esiner, S.; Zhao, J.; Van Assche, G.; Wienk, M. M.; Maes, W.; Lusten, L.; Van Mele, B.; Janssen, R. A. J.; Manca, J.; Vanderzande, D. *J. Mater. Chem.* **2011**, *21*, 8470.
- (29) Bertho, S.; Janssen, G.; Cleij, T. J.; Conings, B.; Moons, W.; Gadisa, A.; D'Haen, J.; Goovaerts, E.; Lutsen, L.; Manca, J.; Vanderzande, D. *Sol. Energy Mater. Sol. Cells* **2008**, *92*, 753.
- (30) Kim, F. S.; Ren, G.; Jenekhe, S. A. *Chem. Mater.* **2011**, *23*, 682.
- (31) Chen, J.-T.; Hsu, C.-S. *Polym. Chem.* **2011**, *2*, 2707.

- (32) Ihn, K. J.; Moulton, J.; Smith, P. J. *Polym. Sci., Part B: Polym. Phys.* **1993**, *31*, 735.
- (33) Kiriya, N.; Jähne, E.; Adler, H.-J.; Schneider, M.; Kiriya, A.; Gorodyska, G.; Minko, S.; Jehnichen, D.; Simon, P.; Fokin, A. A.; Stamm, M. *Nano Lett.* **2003**, *3*, 707.
- (34) Samitsu, S.; Shimomura, T.; Heike, S.; Hashimzume, T.; Ito, K. *Macromolecules* **2008**, *41*, 8000.
- (35) Oosterbaan, W. D.; Vrindts, V.; Berson, S.; Guillerez, S.; Douheret, O.; Ruttens, B.; D'Haen, J.; Adriaensens, P.; Manca, J.; Lusten, L.; Vanderzande, D. *J. Mater. Chem.* **2009**, *19*, 5424.
- (36) Liu, J.; Arif, M.; Zou, J.; Khondaker, S. I.; Zhai, L. *Macromolecules* **2009**, *42*, 9390.
- (37) Xu, W.; Li, L.; Tang, H.; Li, H.; Zhao, X.; Yang, X. *J. Phys. Chem. B* **2011**, *115*, 6412.
- (38) Park, Y. D.; Lee, S. G.; Lee, H. S.; Kwak, D.; Lee, D. H.; Cho, K. *J. Mater. Chem.* **2011**, *21*, 2338.
- (39) Roehling, J. D.; Arslan, I.; Moulé, A. J. *J. Mater. Chem.* **2012**, *22*, 2498.
- (40) Merlo, J. A.; Frisbie, C. D. *J. Polym. Sci., Part B: Polym. Phys.* **2003**, *41*, 2674.
- (41) Samitsu, S.; Shimomura, T.; Heike, S.; Hashizume, T.; Ito, K. *Macromolecules* **2010**, *43*, 7891.
- (42) Kim, F. S.; Jenekhe, S. A. *Macromolecules* **2012**, *45*, 7514.
- (43) Niles, E. T.; Roehling, J. D.; Yamagata, H.; Wise, A. J.; Spano, F. C.; Moulé, A. J.; Grey, J. K. *J. Phys. Chem. Lett.* **2012**, *3*, 259.
- (44) Baghgar, M.; Labastide, J.; Bokel, F.; Dujovne, I.; McKenna, A.; Barnes, A. M.; Pentzer, E.; Emrick, T.; Hayward, R.; Barnes, M. D. *J. Phys. Chem. Lett.* **2012**, *3*, 1674.
- (45) Berson, S.; De Bettignies, R.; Bailly, S.; Guillerez, S. *Adv. Funct. Mater.* **2007**, *17*, 1377.
- (46) Xin, H.; Kim, F. S.; Jenekhe, S. A. *J. Am. Chem. Soc.* **2008**, *130*, 5424.
- (47) Kim, J. S.; Lee, J. H.; Park, J. H.; Shim, C.; Sim, M.; Cho, K. *Adv. Funct. Mater.* **2011**, *21*, 480.
- (48) Rice, A. H.; Giridharagopal, R.; Zheng, S. X.; Ohuchi, F. S.; Ginger, D. S.; Luscombe, C. K. *ACS Nano* **2011**, *5*, 3132.
- (49) He, M.; Zhao, L.; Wang, J.; Han, W.; Yang, Y.; Qiu, F.; Lin, Z. *ACS Nano* **2010**, *4*, 3241.
- (50) Ren, G.; Wu, P.-T.; Jenekhe, S. A. *ACS Nano* **2010**, *5*, 376.
- (51) Ren, G.; Wu, P.-T.; Jenekhe, S. A. *Chem. Mater.* **2010**, *22*, 2020.
- (52) Lee, E.; Hammer, B.; Kim, J.-K.; Page, Z.; Emrick, T.; Hayward, R. C. *J. Am. Chem. Soc.* **2011**, *133*, 10390.
- (53) Hammer, B. A. G.; Bokel, F. A.; Hayward, R. C.; Emrick, T. *Chem. Mater.* **2011**, *23*, 4250.
- (54) Gilroy, J. B.; Lunn, D. J.; Patra, S. K.; Whittell, G. R.; Winnik, M. A.; Manners, I. *Macromolecules* **2012**, *45*, 5806.
- (55) He, M.; Han, W.; Ge, J.; Yang, Y.; Qiu, F.; Lin, Z. *Energy Environ. Sci.* **2011**, *4*, 2894.
- (56) Ge, J.; He, M.; Yang, X.; Ye, Z.; Liu, X.; Qiu, F. *J. Mater. Chem.* **2012**, *22*, 19213.
- (57) Li, F.; Yang, J.; Qin, Y. *J. Polym. Sci., Part A: Polym. Chem.* **2013**, *51*, 3339.
- (58) Li, F.; Yager, K. G.; Dawson, N. M.; Yang, J.; Malloy, K. J.; Qin, Y. *Macromolecules* **2013**, *46*, 9021.
- (59) Johnston, D. E.; Yager, K. G.; Hlaing, H.; Lu, X.; Ocko, B. M.; Black, C. T. *ACS Nano* **2014**, *8*, 243.
- (60) Allen, J. E.; Ray, B.; Khan, M. R.; Yager, K. G.; Alam, M. A.; Black, C. T. *Appl. Phys. Lett.* **2012**, *101*, 063105.
- (61) Johnston, D. E.; Yager, K. G.; Nam, C.-Y.; Ocko, B. M.; Black, C. T. *Nano Lett.* **2012**, *12*, 4181.
- (62) Baker, J. L.; Jimison, L. H.; Mannsfeld, S.; Wolkman, S.; Yin, S.; Subramanian, S.; Salleo, A.; Alivisatos, A. P.; Toney, M. F. *Langmuir* **2010**, *26*, 9146.
- (63) Li, L.; Lu, G.; Yang, X. *J. Mater. Chem.* **2008**, *18*, 1984.
- (64) Sun, S.; Salim, T.; Wong, L. H.; Foo, Y. L.; Boey, F.; Lam, Y. M. *J. Mater. Chem.* **2011**, *21*, 377.
- (65) The original NF solutions were diluted 400 times using the same solvent mixtures in order to avoid detector saturation during UV-vis absorption measurements. This procedure did not seem to lead to redissolution or any apparent changes of the already formed NFs. We have measured the UV-vis absorption of P1 NF solutions upon dilutions ranging from 2 times to 1600 times. Almost identical spectra were observed for all dilutions as shown in Figure S11, indicating these NFs are relatively stable under the current dilution conditions.
- (66) Spano, F. C. *Chem. Phys.* **2006**, *325*, 22.
- (67) Spano, F. C. *Acc. Chem. Res.* **2010**, *43*, 429.
- (68) He, M.; Ge, J.; Fang, M.; Qiu, F.; Yang, Y. *Polymer* **2010**, *51*, 2236.
- (69) Qi, B.; Wang, J. *J. Mater. Chem.* **2012**, *22*, 24315.
- (70) Smilgies, D.-M. *J. Appl. Crystallogr.* **2009**, *42*, 1030.